

# The Megamaser Cosmology Project. VI. Observations of NGC 6323

C. Y. Kuo<sup>1</sup>, J. A. Braatz<sup>2</sup>, K. Y. Lo<sup>2</sup>, M. J. Reid<sup>3</sup>, S. H. Suyu<sup>1</sup>, D. W. Pesce<sup>4</sup>, J. J. Condon<sup>2</sup>, C. Henkel<sup>5,6</sup>, C. M. V. Impellizzeri<sup>2</sup>

<sup>1</sup>*Academia Sinica Institute of Astronomy and Astrophysics, P.O. Box 23-141, Taipei 10617, Taiwan*

<sup>2</sup>*National Radio Astronomy Observatory, 520 Edgemont Road, Charlottesville, VA 22903, USA*

<sup>3</sup>*Harvard-Smithsonian Center for Astrophysics, 60 Garden Street, Cambridge, MA 02138, USA*

<sup>4</sup>*Department of Astronomy, University of Virginia, Charlottesville, VA 22904*

<sup>5</sup>*Max-Planck-Institut für Radioastronomie, Auf dem Hügel 69, 53121 Bonn, Germany*

<sup>6</sup>*Astronomy Department, Faculty of Science, King Abdulaziz University, P.O. Box 80203, Jeddah, Saudi Arabia*

## ABSTRACT

We present observations of the H<sub>2</sub>O megamasers in the accretion disk of NGC 6323. By combining interferometric and spectral monitoring data, we estimate  $H_0 = 73^{+26}_{-22}$  km/s/Mpc, where the low strength of the systemic masers ( $< 15$  mJy) limits the accuracy of this estimate. The methods developed here for dealing with weak maser emission provide guidance for observations of similar sources, until significant increases in radio telescope sensitivity, such as anticipated from the next generation Very Large Array, are realized.

*Subject headings:* accretion, accretion disks – galaxies: nuclei – galaxies: masers – galaxies: active – galaxies: ISM – galaxies: Seyfert

## 1. INTRODUCTION

H<sub>2</sub>O megamasers provide a direct determination of  $H_0$  independent of standard candles (e.g. Reid et al. 2009, Braatz et al. 2010, Reid et al. 2013, Kuo et al. 2013). This method involves sub-milliarcsecond resolution imaging of H<sub>2</sub>O maser emission from sub-parsec circumnuclear disks at the center of active galaxies, and the *geometric* distance to each of the galaxies is determined based on measurements of the orbital size and velocity as well as the centripetal acceleration of maser clouds orbiting around the supermassive black hole. Since this technique involves very few assumptions and can be applied to maser galaxies in the Hubble flow in a single step, systematic errors are expected to be small. In the Megamaser Cosmology Project (MCP), we have currently obtained a  $H_0$  of  $68 \pm 7$  km s<sup>-1</sup> Mpc<sup>-1</sup> from UGC 3789 (Reid et al. 2013) and  $68 \pm 11$  km s<sup>-1</sup> Mpc<sup>-1</sup> from NGC 6264 (Kuo et al. 2013). To further constrain  $H_0$ , we are currently measuring additional maser galaxies and searching for more high quality megamaser disk systems which are suitable for  $H_0$  determination.

In this paper, we present observations of NGC 6323, a Seyfert 2 galaxy at a distance of  $\sim 100$  Mpc. The masers in this galaxy shows a Keplerian rotation curve and have the necessary maser components (i.e. the systemic and high-velocity masers; see Kuo et al. 2011 for their definitions) for a  $H_0$  determination with the H<sub>2</sub>O megamaser technique. It is different from our previously published maser galaxies (i.e. UGC 3789 and

NGC 6264) in that the systemic masers, are quite weak. The typical signal-to-noise ratio (SNR) of a systemic maser line is only  $\sim 10$  in spectra taken by the Green Bank Telescope (GBT) <sup>1</sup> with an integration time of  $\approx 3$  hours. Since the SNR of the systemic masers plays a crucial role in the precision of the  $H_0$  estimate, NGC 6323 provides a test case to explore the accuracy and precision one can achieve in determining  $H_0$  from a galaxy with faint systemic masers.

In section 2, we present our VLBI and single-dish observations. In section 3, we show the analysis of the centripetal accelerations of the masers in NGC 6323. The analyses of the Hubble constant determination are presented in section 4. Finally, we summarize the results in section 5.

## 2. Observations and Data Reduction

### 2.1. GBT monitoring

We observed the H<sub>2</sub>O maser in NGC 6323 with the GBT at 21 epochs between 2006 October 30 and 2009 May 19. Except during the summer months when the humidity makes observations at 22 GHz inefficient, we took a spectrum on a monthly timescale. For these observations, we followed the same observing settings and data reduction procedures as in Braatz et al. (2010). Table 1 shows the observing date and sensitivity for each observation. Figure 1 shows a representative H<sub>2</sub>O maser spectrum for NGC 6323.

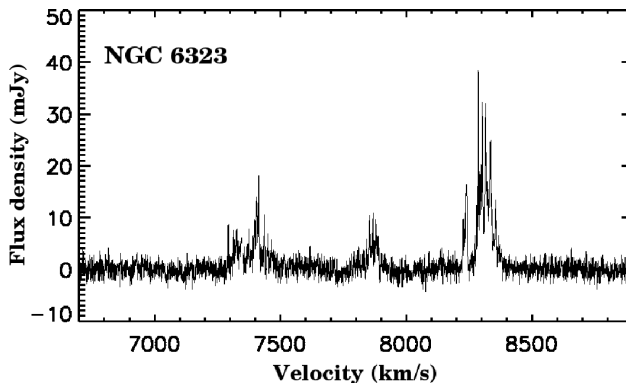


Fig. 1.— A characteristic H<sub>2</sub>O maser spectrum of NGC 6323 obtained on 2007 April 6. The vertical axis is flux density in mJy and the horizontal axis is Local Standard of Rest velocity (optical definition). Note that the systemic maser emission between  $\approx 7800$  and  $7900 \text{ km s}^{-1}$  is weak ( $< 10 \text{ mJy}$ ).

### 2.2. VLBI Data

We observed NGC 6323 with thirteen 12-hour tracks of VLBI observations between 2007 and 2009 using the Very Long Baseline Array (VLBA)<sup>2</sup>, augmented by the 100-m Green Bank Telescope and the

<sup>1</sup>The Green Bank Telescope is a facility of the National Radio Astronomy Observatory.

<sup>2</sup>The VLBA is a facility of the National Radio Astronomy Observatory, which is operated by the Associated Universities, Inc. under a cooperative agreement with the National Science Foundation (NSF).

100-m Effelsberg telescope <sup>3</sup>. These observations have been presented in Kuo et al. (2011), who used the interferometric maps to estimate the supermassive black hole mass, using a distance given by assuming  $H_0 = 73 \text{ km s}^{-1} \text{ Mpc}^{-1}$  and a recessional velocity of  $7848 \text{ km s}^{-1}$ .

We have improved on the previous analysis by dividing the calibrated interferometer (u,v)-data into yearly groups, periods A, B, and C (see Table 1), merging data within a group, and then imaging. We could not combine all the data when imaging, since most maser spots changed amplitude significantly over the three year span of the observations. By comparing maser positions from different periods, we can estimate the magnitude of systematic position offsets in the maser astrometry, owing to independent phase and delay calibration. When comparing maser positions, we use the data from period C as the reference because we have the most complete data in this period and this data dominate the sensitivity of the entire dataset. We found that there is no systematic offset between maser positions measured in period A and C, and the average maser positions from these two periods agree within  $2 \mu\text{as}$ . However, when comparing positions measured from periods B and C, we found systematic position offsets for the systemic and blueshifted masers. There is no position offset for the redshifted masers in period B and C as expected because all maser positions are referenced to the average position of the redshifted masers as a result of the self-calibration process.

The average position of the systemic masers in period B has an offset of  $1 \pm 5 \mu\text{as}$  in the easterly ( $x$ ) direction and  $10 \pm 8 \mu\text{as}$  in the northerly ( $y$ ) direction from that of the systemic masers in period C. For the blueshifted masers, the average offsets in  $x$  and  $y$  between period B and C are  $7 \pm 4 \mu\text{as}$  and  $22 \pm 8 \mu\text{as}$ , respectively. Since the systemic and blueshifted masers have average frequency offsets of 31 MHz and 64 MHz, respectively, from the average frequency of the spectral channels of the redshifted masers used for self-calibration, the systematic position offsets in the  $y$  direction appear to be frequency dependent in nature, implying a residual error of  $\sim 0.4 \text{ nsec}$  in the multiband delay calibration for our VLBI data taken in period B. In order to reduce the systematic error caused by these systematic position offsets in the model fitting described in Section 4, we corrected for these offsets in the maser positions measured in period B before performing disk modeling and Hubble constant determination.

Next, we averaged the maser positions from the three periods to further increase position precision. Evidence from other (stronger) megamasers (NGC 4258 and UGC 3789) supports the assumption that over time periods of a few years, the location and acceleration of maser spots at any given velocity are nearly constant, even though their amplitudes can vary. The physical model of megamasers that is best supported by all observations (e.g. Humphreys et al. 2008, Reid et al. 2013, Kuo et al. 2013) is that there is spiral structure in the accretion disk, and typically one or two arms produce detectable maser emission. Since, we observe the masers for only about 0.1% of a maser orbital period, little change in position or acceleration would be expected. In Table 2, we show the positions and velocities of all maser spots used for the disk modeling. (Throughout this paper, maser velocities mentioned are referenced to the Local Standard of Rest (LSR), using the optical velocity convention, even though full relativistic corrections are used when modeling).

---

<sup>3</sup>The Effelsberg 100-m telescope is a facility of the Max-Planck-Institut für Radioastronomie.

Table 1. GBT Observing dates and sensitivities for NGC 6323

Epoch	Date	Day Number	$T_{sys}$ (K)	rms Noise (mJy)	Period
0	2006 October 30	0	42.4	2.2	A
1	2006 December 2	33	36.0	1.4	A
2	2007 February 22	115	44.0	2.2	A
3	2007 April 6	158	35.9	1.8	A
4	2007 October 29	364	34.3	1.4	B
5	2007 November 28	394	35.7	1.6	B
6	2007 December 26	422	55.0	2.9	B
7	2008 February 2	460	39.3	1.5	B
8	2008 February 29	487	44.0	1.7	B
9	2008 March 25	512	34.2	1.3	B
10	2008 April 24	542	56.5	1.8	B
11	2008 May 6	554	41.1	2.4	B
12	2008 May 29	577	49.4	2.0	B
13	2008 September 29	700	47.7	2.2	C
14	2008 October 31	732	43.5	1.7	C
15	2008 November 28	760	35.9	1.1	C
16	2008 December 29	791	35.2	1.3	C
17	2009 January 30	823	33.8	1.1	C
18	2009 March 4	856	31.5	1.2	C
19	2009 March 31	883	38.2	1.3	C
20	2009 May 19	932	35.3	1.5	C

Note. — The sensitivities are calculated without performing Hanning smoothing to the spectra and are based on  $0.33 \text{ km s}^{-1}$  channels. We label Period A, B, and C to those times when we have continuous observations on a monthly timescale. These periods are separated by summer months during which the humidity makes observations inefficient.

Table 2. Maser Position, Velocity, and Acceleration Data for NGC 6323

$V_{\text{op}}^{\text{a}}$ (km s <sup>-1</sup> )	$\Theta_x^{\text{b}}$ (mas)	$\sigma_{\Theta_x}^{\text{b}}$ (mas)	$\Theta_y^{\text{b}}$ (mas)	$\sigma_{\Theta_y}^{\text{b}}$ (mas)	$A^{\text{c}}$ (km s <sup>-1</sup> yr <sup>-1</sup> )	$\sigma_A^{\text{c}}$ (km s <sup>-1</sup> yr <sup>-1</sup> )
8372.94	-0.021	0.009	-0.308	0.019	...	...
8365.82	-0.023	0.007	-0.274	0.014	...	...
8362.25	-0.035	0.010	-0.338	0.021	...	...
8358.69	-0.033	0.007	-0.323	0.012	...	...
8355.13	-0.030	0.004	-0.316	0.006	...	...
8351.57	-0.026	0.003	-0.317	0.006	...	...
8348.01	-0.023	0.004	-0.341	0.007	...	...
8344.44	-0.031	0.008	-0.332	0.016	...	...
8340.88	-0.027	0.005	-0.353	0.010	...	...
8337.32	-0.048	0.002	-0.364	0.004	...	...
8333.76	-0.047	0.002	-0.370	0.003	-0.22	0.25
8330.20	-0.051	0.002	-0.369	0.004	...	...
8326.63	-0.049	0.002	-0.382	0.004	-0.58	0.36
8323.07	-0.047	0.002	-0.370	0.004	-0.40	0.38
8319.51	-0.051	0.002	-0.364	0.003	-0.04	0.36
8315.95	-0.048	0.002	-0.368	0.003	0.11	0.36
8312.38	-0.056	0.002	-0.384	0.003	0.07	0.41
8308.82	-0.056	0.004	-0.383	0.007	-0.17	0.41
8305.26	-0.065	0.002	-0.407	0.004	...	...
8301.70	-0.064	0.002	-0.418	0.003	-0.06	0.30
8298.13	-0.065	0.002	-0.425	0.004	...	...
8294.57	-0.065	0.002	-0.430	0.003	-0.04	0.27
8291.01	-0.062	0.002	-0.430	0.004	0.00	1.00
8287.45	-0.063	0.002	-0.432	0.003	0.11	0.24
8283.89	-0.062	0.002	-0.433	0.003	0.00	1.00
8280.32	-0.062	0.002	-0.416	0.003	-0.16	0.24
8276.76	-0.071	0.003	-0.456	0.006	...	...
8273.20	-0.068	0.006	-0.446	0.011	...	...
8269.64	-0.073	0.009	-0.426	0.015	...	...
8258.95	-0.071	0.006	-0.494	0.010	...	...
8241.14	-0.089	0.003	-0.516	0.006	...	...
8237.58	-0.090	0.002	-0.521	0.004	...	...
8234.01	-0.096	0.002	-0.511	0.005	...	...
8230.45	-0.098	0.004	-0.513	0.007	...	...
8226.89	-0.096	0.003	-0.537	0.006	-0.40	0.39
8223.33	-0.101	0.004	-0.543	0.007	...	...
7885.90	-0.009	0.005	-0.014	0.009	1.49	0.41

Table 2—Continued

$V_{\text{op}}^{\text{a}}$ (km s <sup>-1</sup> )	$\Theta_x^{\text{b}}$ (mas)	$\sigma_{\Theta_x}^{\text{b}}$ (mas)	$\Theta_y^{\text{b}}$ (mas)	$\sigma_{\Theta_y}^{\text{b}}$ (mas)	$A^{\text{c}}$ (km s <sup>-1</sup> yr <sup>-1</sup> )	$\sigma_A^{\text{c}}$ (km s <sup>-1</sup> yr <sup>-1</sup> )
7882.35	-0.000	0.004	-0.016	0.007	0.84	0.26
7878.80	0.001	0.004	-0.016	0.007	0.63	0.25
7875.25	-0.002	0.005	-0.010	0.008	0.89	0.20
7868.14	0.002	0.004	0.000	0.006	0.79	0.14
7864.59	0.004	0.005	-0.017	0.009	1.12	0.15
7853.93	-0.002	0.004	0.000	0.008	1.27	0.54
7850.38	0.001	0.006	0.028	0.011	0.80	0.24
7846.83	0.002	0.004	0.009	0.005	1.07	0.11
7843.27	-0.004	0.010	-0.030	0.023	1.07	0.11
7804.19	0.011	0.012	0.016	0.021	1.47	0.27
7465.43	0.120	0.005	0.550	0.009	0.05	0.24
7447.73	0.118	0.004	0.504	0.008	-0.11	0.24
7437.10	0.093	0.004	0.483	0.007	...	...
7433.56	0.093	0.003	0.461	0.006	...	...
7415.85	0.097	0.003	0.387	0.005	...	...
7412.31	0.091	0.002	0.394	0.003	0.39	0.42
7408.77	0.087	0.003	0.405	0.005	...	...
7405.23	0.090	0.002	0.406	0.005	0.04	0.42
7401.69	0.093	0.004	0.415	0.006	...	...
7398.15	0.090	0.004	0.412	0.007	...	...
7394.60	0.083	0.005	0.424	0.010	...	...
7373.36	0.070	0.007	0.345	0.013	...	...
7369.81	0.066	0.009	0.341	0.020	...	...
7345.02	0.058	0.006	0.342	0.012	...	...
7337.94	0.054	0.006	0.334	0.010	...	...
7330.86	0.049	0.008	0.314	0.015	...	...
7327.32	0.047	0.006	0.300	0.010	...	...
7323.78	0.055	0.005	0.286	0.010	...	...
7320.23	0.052	0.006	0.286	0.011	...	...
7316.69	0.058	0.007	0.266	0.014	...	...
7313.15	0.047	0.008	0.283	0.017	...	...

Note. —

<sup>a</sup>Velocity referenced to the LSR and using the optical definition (no relativistic corrections).

<sup>b</sup>East-west and north-south position offsets and uncertainties. Position uncertainties reflect fitted random errors only.

<sup>c</sup>Measured or estimated acceleration and its uncertainty for each maser component.

### 3. Acceleration Analysis

Following Kuo et al. (2013), we adopted two approaches to measure accelerations of maser spots: initial estimates from the *eye-tracking* method for high velocity masers followed by two methods of *global least-squares fitting* (Humphreys et al. 2008; Braatz et al. 2010; Reid et al. 2013; Kuo et al. 2013) for systemic masers. In essence, the eye-tracking approach yields estimates of acceleration by fitting a straight line to spectral peak velocities, identified by eye from the spectra, as a function of time. The global least-squares fitting method fits the amplitudes for a range of channels in all selected spectra simultaneously, with a model consisting of multiple Gaussian-shaped lines that drift linearly in time.

#### 3.1. High Velocity Masers

In Figure 2, we plot the radial velocities of the high-velocity maser peaks as a function of time. Note that while the blueshifted and redshifted maser lines are distributed over a velocity range of  $\sim 200 \text{ km s}^{-1}$ , not all maser features are represented in Figure 2. This is because maser lines blend with their neighboring maser features significantly. To measure the accelerations of the maser features seen in Figure 2, we first identify the lines that are persistent in time and then fit a straight line to the data to measure the accelerations directly. The uncertainty of the measurements is estimated by scaling the fitting error by the square root of reduced  $\chi^2$ .

The variance weighted average accelerations of the redshifted and blueshifted masers are  $-0.14$  and  $-0.01 \text{ km s}^{-1} \text{ yr}^{-1}$  respectively. The rms scatter of accelerations of the redshifted and blueshifted masers are  $0.26$  and  $0.21 \text{ km s}^{-1} \text{ yr}^{-1}$ . The small accelerations and rms scatter indicate that the high velocity masers are close to the mid-line of the accretion disk as expected. To account for possible uncertainty caused by line blending, we use the rms scatter of the acceleration measurement as an estimate of the systematic error and include this error in the total uncertainty before performing disk modeling described in Section 4. Fitted accelerations and uncertainties that include the systematic errors are listed in Table 2.

#### 3.2. Systemic Masers

The systemic features of NGC 6323 have low signal-to-noise ratios (SNRs) and significant line-blending that make acceleration fitting difficult. To facilitate more reliable and stable acceleration fitting, we follow Kuo et al. (2013) and separate the maser lines into velocity sub-groups having similar apparent accelerations. Assignment to an acceleration sub-group was done by examining *dynamic spectra* to identify persistent patterns. Dynamic spectra plot the flux density as color-coded intensity as a function of velocity versus time (see Figure 3). Flux densities were interpolated between monthly monitoring gaps, but not across longer (summer) gaps. Based on the dynamic spectra, we identify seven groups of masers that show coherent drifting patterns. Then, we estimated accelerations for the maser features in each group separately with global least-squares fitting.

When fitting the spectra for accelerations, we divide the data into periods based on seeing coherent drifting patterns in the dynamic spectra. We show the epochs used in the acceleration fitting for all maser groups in the 3rd column in Table 3. Note that we were unsuccessful fitting for masers in Group 5 and 6 between epochs 14 (Day 732) through 20 (Day 932), as a result of low SNR, severe line-blending, and especially the short time baseline.



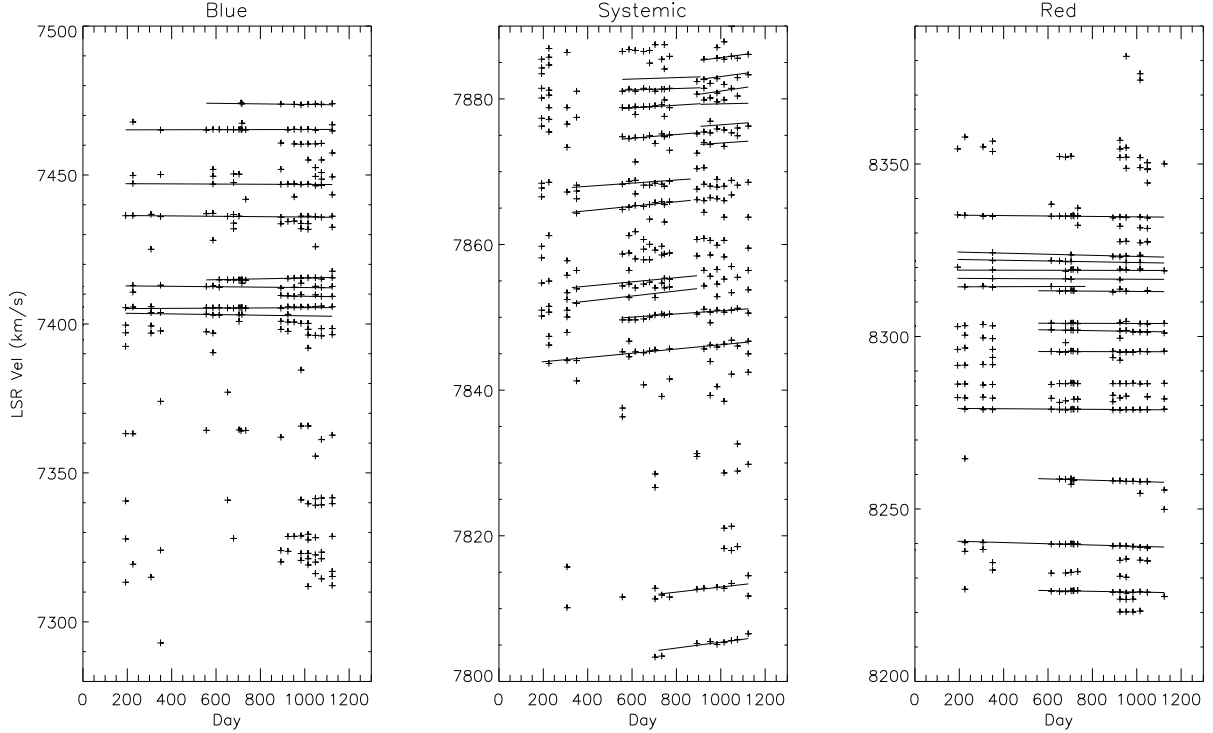


Fig. 2.— We plot the radial velocities of NGC 6323 maser peaks as a function of time (the crosses) for the blue-shifted masers (the left panel), the systemic masers (the middle panel), and the red-shifted masers (the right panel). On top of these plots, we overplot the fitting results from the eye-tracking method for the high-velocity masers and from the least-squares fitting for the systemic masers. The data between Day 100 and 400 come from spectra taken in Period A; the data between Day 500 to 800 from spectra in Period B; and the data between Day 800 to 1200 are from spectra in Period C.

We followed *Method 1* and *Method 2* described in Reid et al. (2013) to fit the accelerations of the systemic masers. These methods differ in the choice of initial parameter values and the number of Gaussian components used. Also, Method 1 allows each Gaussian component to have independently estimated accelerations, whereas Method 2 assumes maser accelerations are a linear function of velocity, defined as a single acceleration ( $A_{sys}$ ) at the center of the velocity range and its velocity derivative ( $dA_{sys}/dv$ ). The difference between the measurements from these two methods allows an estimate of uncertainty in measured acceleration, based on fitting methodology.

In Figure 4, we show the results of the acceleration measurements using both methods. Overall, the measurements from the two methods agree very well, as do the accelerations obtained from the same group fitted over different periods of time. For the disk fitting presented in Section 4, we adopted the acceleration measurements from Method 1 (see Table 3), because this method makes less restrictive assumptions. Typical reduced  $\chi^2_\nu$  values for these fits are 0.92-1.13 for all maser groups except for Group 4, which typically had  $\chi^2_\nu \approx 1.36$ . Only for the weak masers with velocities between 7882 and 7885 km s<sup>-1</sup> do we see a marginally significant difference between measurements made between epochs 4–13 (in group 7a) and 14–20 (in group

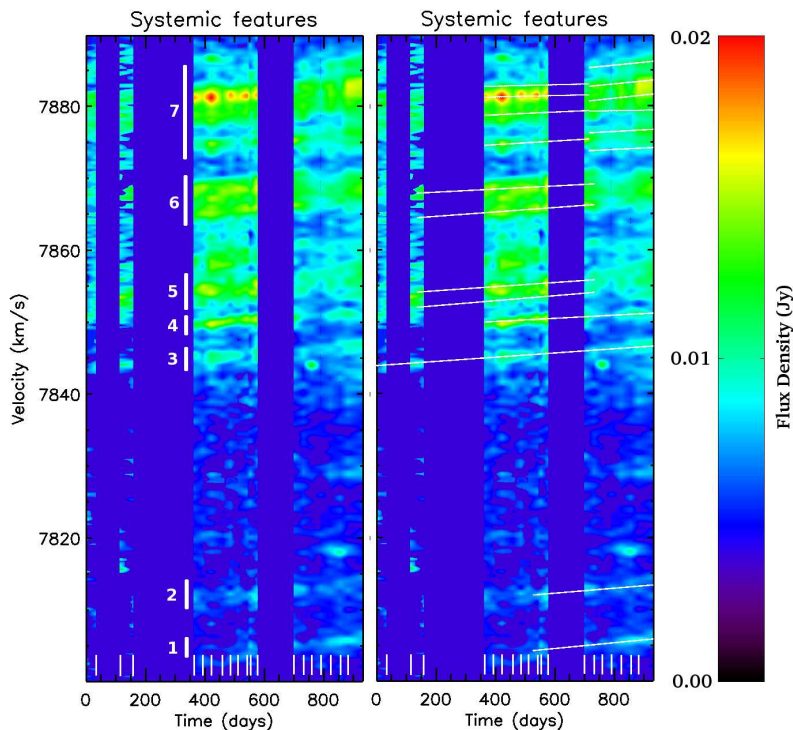


Fig. 3.— Dynamic spectra of the systemic masers in NGC 6323. The left panel shows the maser flux density as a function of time and velocity. The white ticks at the bottom of the figure show the epochs at which we took the maser spectra. Except for epochs separated by a summer gap, the maser flux at the time between these epochs is obtained by linearly interpolating the flux densities measured in consecutive epochs. No interpolation is used for consecutive spectra that are separated by a summer gap (i.e. Day 160-360 and Day 580-700), and these regions are intentionally left blank. The vertical white lines in the figure show the velocity windows in which we can see clear drifting pattern of maser lines and the accelerations of the maser components within the window can be assumed to be approximately the same. The numbers adjacent to the white lines are the group numbers we assign to the velocity windows. In the right panel, we overplot the straight lines that represent the best-fit accelerations from the least-squares fitting on the plot shown in the left panel.

7b). For this velocity range we adopt the variance weighted average of the two measurements. In Section 4, we will explore the systematic uncertainty in  $H_0$  caused by the slightly discrepant acceleration measurements for masers in group 7a and 7b.

## 4. Modeling the Accretion Disk and Determining $H_0$

### 4.1. Disk Modeling

The Hubble constant determination with the disk modeling method developed in Reid et al. (2013) relies on modeling the sub-parsec scale maser disk in three dimensions and adjusting model parameters to minimize the position, velocity, and acceleration residuals for each maser spot. Global model parameters include  $H_0$ , black hole mass ( $M$ ), recession velocity of the galaxy ( $V_0$ ), and other parameters that describe

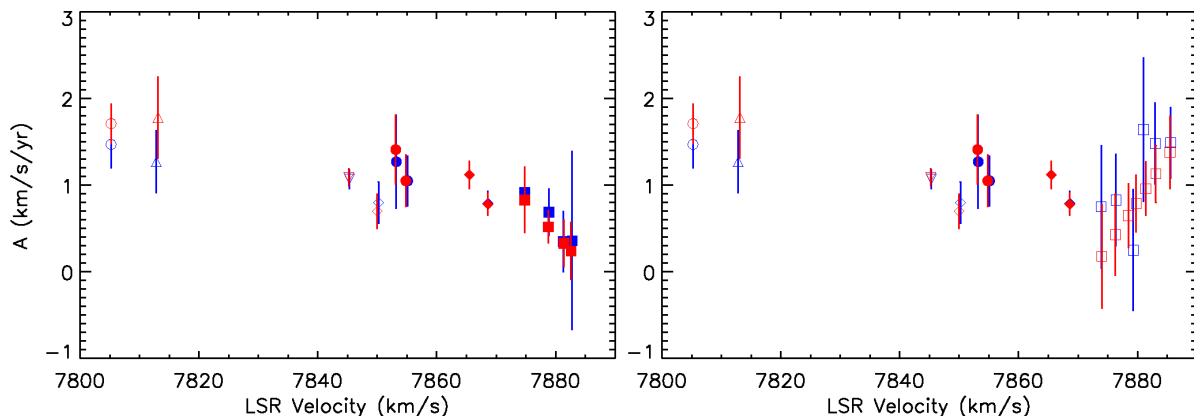


Fig. 4.— The left panel shows the centripetal acceleration of the systemic masers measured from the global least-squares fitting method. The red data points show the measurement assuming that the maser acceleration is a linear function of maser velocity (Method 2, Sect. 3.2.1) whereas the blue ones show the measurement without such an assumption (Method 1, Sect. 3.2.2). The measurements shown in the right panel are the same as the ones shown in the left panel except in the velocity range between  $7873 \text{ km s}^{-1}$  and  $7888 \text{ km s}^{-1}$ . We have different accelerations in this velocity window because we measure the acceleration in two different sets of epochs. The left panel show the measurements using spectra measured between epoch 0 and 13 (Day 0 – Day 700; Group 7a; see also Table 4); the right panel shows the measurement using data taken between epoch 14 and 20 (Day 732 – Day 932; Group 7b).

the orientation and warping of the disk. Key elements for estimating  $H_0$  are the Keplerian position-velocity (rotation) curve described by the high velocity masers, the centripetal accelerations of the systemic masers, and their angular offsets and velocities relative to the dynamical center. In essence, the Keplerian rotation of the disk measured from high-velocity masers determines  $M/D$ , where  $D$  is the distance to the galaxy and  $M$  is the black hole mass, whereas the position, velocity, and acceleration information of the systemic masers give  $M/D^2$  (see Kuo et al. 2013). Therefore, one can measure  $D$  by solving the above two equations, and  $H_0$  can be directly inferred from  $D$  and the galaxy’s Hubble flow speed,  $V_0$ , also obtained from the high-velocity rotation curve. We refer the readers to Reid et al. (2012) and Kuo et al. (2013) for detailed information of the disk modeling.

In the disk modeling, we associated maser positions and velocities with accelerations measured from the GBT monitoring of maser spectra by choosing the VLBI channel with the velocity closest to that of an acceleration fit. For the high velocity masers, since there are fewer acceleration fits than VLBI measurements of maser position and velocity as results of the line-blending effect and of using the eye-tracking method to measure the acceleration of high-velocity masers, not all VLBI measurements have corresponding accelerations. For maser features without acceleration measurements, we use only the position and velocity data in the disk modeling. We show the input data (including the velocity, position, and acceleration for each maser feature) for the disk modeling in Table 2.

Rather than using formal fitting uncertainties for maser position and velocity, which tend to be optimistic, we added estimates of systematic uncertainty (“error floors”) in quadrature with the formal uncertainties. For the  $x$ - and  $y$ -data, we followed Reid et al. (2013) to adopt an error floor of 0.01 mas. For maser velocity, the precise value for the error floor is not important, because it only affects the convergence rate of the disk fitting and does not affect the best-fit result. Therefore, as a rough estimate of the systematic error for maser velocity, we adopt  $1.8 \text{ km s}^{-1}$  ( $\approx 1/2$  of the velocity channel width).

We adopt a peculiar (deviation from a pure Hubble flow) velocity of  $-285 \pm 163 \text{ km s}^{-1}$  for NGC 6323 (Masters; private communication). This comes from galaxy flow models of the local supercluster (Masters 2005). Note that this peculiar velocity is relatively small, because toward the Perseus-Pisces supercluster deviations from Hubble’s flow are modest. Given the recession velocity of NGC 6323 is  $\sim 7800 \text{ km s}^{-1}$ , the precise value of the peculiar velocity is unimportant as it contributes only  $\approx 2\%$  to the total  $H_0$  uncertainty.

We modeled the maser disk in 3 dimensions with the same 10 global parameters used in modeling the maser disk in UGC 3789 (Reid et al. 2013) and perform the model fitting with a Markov Chain Monte Carlo (MCMC) approach (e.g. Geyer 1992; Gilks, Richardson & Spiegelhalter 1996) to obtain the posteriori probability density distributions of the model parameters. Optimum values of the model parameters were estimated from the *posteriori* probability density functions (PDFs), marginalized over all other parameters. To verify convergence of the MCMC fitting, we adopted the power-spectrum method by Dunkley et al. (2005). In this method, one measures the variance of the mean of the probability distribution and the correlation length of the MCMC chain from its power spectrum, followed by evaluation of the degree of convergence based on these two parameters. A MCMC chain is considered to have converged if  $r < 0.01$  and  $j^* \geq 20$ . Here,  $r$  is the convergence ratio, defined as the ratio between the variance of the sample mean and variance of the underlying probability distribution ( $\sigma_x^2/\sigma_0^2$ ), and  $j^* = k^*(N/2\pi)$  indicates the region in the power spectrum (i.e. the wavenumber  $k^*$ ) of the MCMC chain where the chain starts to deviate from the white noise regime (see Dunkley et al. 2005 for details).  $N$  in the above expression for  $j^*$  is the total number of samples in the MCMC chain. Finally, our estimates of the best global parameter values come from the marginalized PDFs; we adopted the median of the marginalized PDF, with the uncertainties showing the 16th and 84th percentiles (spanning the 68% confidence interval).

#### 4.2. $H_0$ Estimation

To fully explore the parameter space, we ran 10 independent MCMC chains with different starting conditions. In particular, we choose the starting value for  $H_0$  uniformly in the range  $60 < H_0 < 80 \text{ km s}^{-1} \text{ Mpc}^{-1}$ . The length of each independent run was set to be  $10^8$  MCMC trials. The combined MCMC chains from the 10 independent runs fully satisfied the convergence criteria set by Dunkley et al. (2005), with convergence ratio  $r = 0.0007$  and  $j^* = 33$ .

Figure 5 shows the results of the Bayesian fitting by comparing the most-probable MCMC trial model with the observed maser map, the position-velocity diagram, and the acceleration measurements. In Figure 6, we show the *model* maser distribution from a view along the disk spin axis (left panel) and the warping structure with a nearly edge on view (right panel). In general, the model matches the observations well, and the differences between the data and model are consistent within realistic uncertainties except for a few high-velocity maser spots with relatively large acceleration (i.e.  $\sim -0.6 \text{ km s}^{-1} \text{ yr}^{-1}$ ; see the bottom panel of Figure 5). The total reduced  $\chi^2$  ( $\chi_\nu^2$ ) of the fit is 1.352 for 107 degrees of freedom (291 data points). We summarize the most-probable values for all model parameters in Table 4. Note that since  $\chi_\nu^2 > 1$ , we follow our conservative practice of inflating parameter uncertainties by  $\sqrt{\chi_\nu^2}$ .

We show the posteriori PDF for  $H_0$  from the Bayesian fitting in Figure 7. The PDF is slightly asymmetric about the peak of the distribution at  $H_0 = 67 \text{ km s}^{-1} \text{ Mpc}^{-1}$ . The median of this PDF is  $73 \text{ km s}^{-1} \text{ Mpc}^{-1}$  and the 16th and 84th percentiles span  $51$  to  $99 \text{ km s}^{-1} \text{ Mpc}^{-1}$ . From the fitted recessional velocity of  $7853.4 \pm 2.2 \text{ km s}^{-1}$ , the corresponding distance to NGC 6323 is  $D = V_0/H_0 = 107_{-29}^{+42} \text{ Mpc}$ .

Note that in Section 3.2 we show that there is a marginally significant discrepancy in the acceleration

measurements for group 7a and group 7b, especially at the high end of the velocity window (see Figure 4). To explore the magnitude of the systematic error in  $H_0$  caused by the systematic uncertainty in acceleration, we perform the disk modeling again without including the systemic maser feature with velocity at 7885.9 km s<sup>-1</sup> in Table 2. The resultant  $H_0$  is  $68^{+26}_{-21}$  km s<sup>-1</sup> Mpc<sup>-1</sup>. One can see that the  $H_0$  decreases by 5 km s<sup>-1</sup> Mpc<sup>-1</sup> and this represents the maximum systematic error in  $H_0$  that the discrepant acceleration measurements for the maser features in group 7 at the high velocity end can introduce. Since this number is significantly smaller than the current measurement error in  $H_0$ , one can infer that the systematic error in the accelerations for group 7 has little impact on our current  $H_0$  estimate which is dominated by measurement error.

### 4.3. Sources of Uncertainties in $H_0$

In the context of a thin maser disk with well-measured Keplerian rotation curve, as those cases shown in Kuo et al. (2011), the precision of the  $H_0$  measurement with the megamaser technique relies primarily upon the precision of position and acceleration measurement of the systemic masers. In addition, the spatial and velocity range over which systemic masers can be detected also plays an important role.

For the maser disk in NGC 6323, the large  $H_0$  uncertainty (compared to other MCP galaxies) primarily results from the lower precision of the maser position measurements, owing to weaker maser emission and the fact that the maser disk orients in the north-south direction where we have the poorest angular resolution. The accuracy of acceleration measurements is sufficient so that it is not a dominant contributor to the  $H_0$  uncertainty.

Besides position accuracy, the narrower velocity range of detectable systemic masers in NGC 6323 is also a limiting factor for an accurate  $H_0$  measurement. The velocity range covered by the maser spots with position measurements to better than  $\pm 10 \mu\text{as}$  is less than 50 km s<sup>-1</sup>, whereas in NGC 4258 (Humphreys et al. 2008) and UGC 3789 (Reid et al. 2013) the corresponding velocity ranges are  $\approx 100$  km s<sup>-1</sup>. Therefore, for NGC 6323 our constraints on  $H_0$  are quite limited.

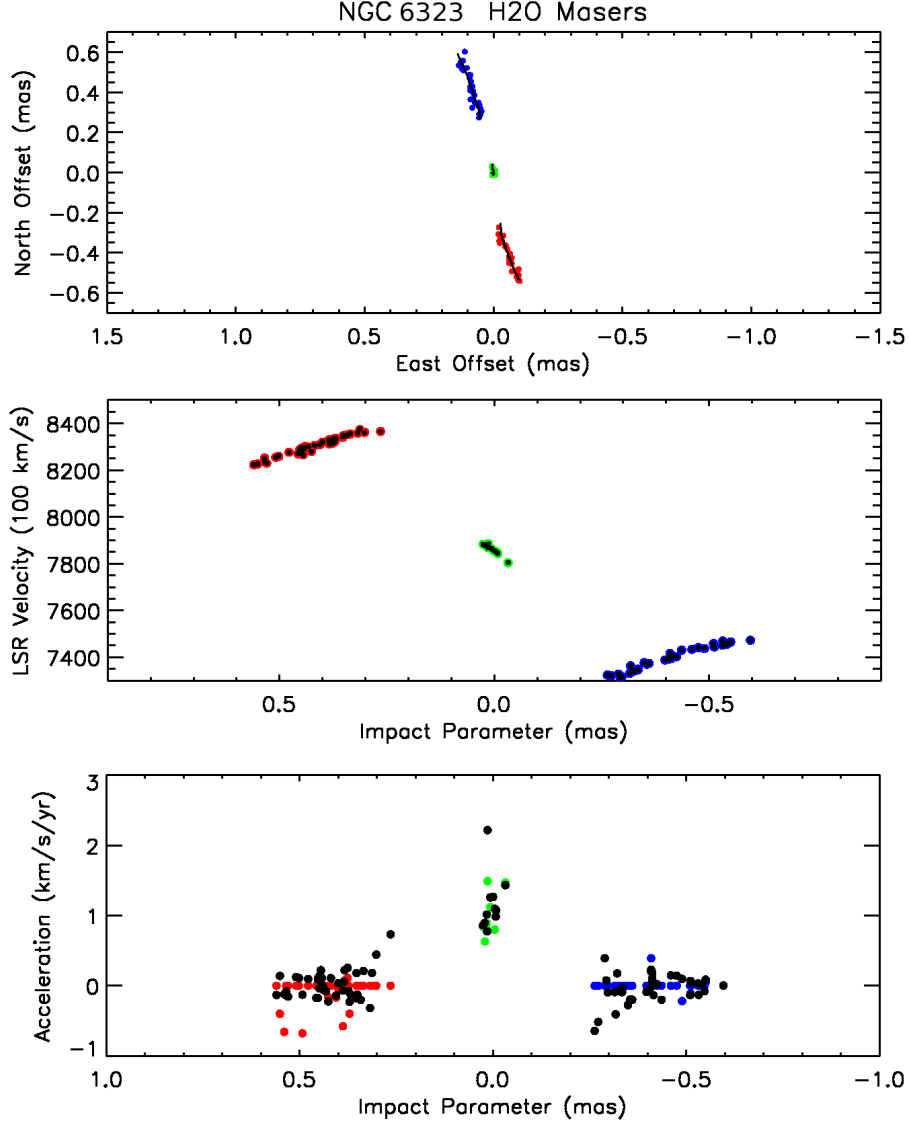


Fig. 5.— Data (colored dots) and best-fit model (lines and black dots). Top panel: Positions on the sky. Middle panel: LSR velocity versus position along the disk. Bottom panel: Accelerations versus impact parameter. In all three panels, the red, green, and blue dots show the redshifted masers, the systemic masers, and the blueshifted masers, respectively. Note that in the bottom panel, there are three redshifted maser spots with acceleration below  $-0.5 \text{ km s}^{-1} \text{ yr}^{-1}$ , which are larger than the typical acceleration (i.e.  $\sim 0 \text{ km s}^{-1} \text{ yr}^{-1}$ ) for high-velocity masers and these values are very likely a result of severe line-blending. Excluding these maser features does not change the  $H_0$  from the disk modeling because the  $H_0$  determination is dominated by the systemic masers. The accelerations of the high-velocity masers play a negligible role in the  $H_0$  measurement.

## 5. Summary

This work presents the third  $H_0$  estimate from the Megamaser Cosmology Project (MCP). Unfortunately, the low flux densities of the systemic masers in NGC 6323 preclude an accurate estimate of  $H_0$ . We discussed several approaches for handling low signal to noise data, but conclude that with current telescope

Table 3. Acceleration Measurements for the Systemic Masers

Group	Velocity (km s <sup>-1</sup> )	Epochs	Ref. Epoch	Linewidth Components	Acceleration (km s <sup>-1</sup> yr <sup>-1</sup> )	$A_\sigma$ (km s <sup>-1</sup> yr <sup>-1</sup> )
1	7805.2	10–20	15	2.6	1.47	0.27
2	7812.8	10–20	15	1.8	1.27	0.36
3	7845.3	0–20	8	1.8	1.07	0.11
4	7850.2	4–20	8	1.7	0.80	0.24
5	7853.2	3–13	8	2.9	1.27	0.54
5	7855.1	3–13	8	2.2	1.05	0.29
6	7865.5	3–14	8	2.7	1.12	0.15
6	7868.6	3–14	8	2.7	0.79	0.14
7a	7874.8	4–13	8	2.9	0.92	0.23
7a	7878.9	4–13	8	2.9	0.69	0.27
7a	7881.3	4–13	8	1.8	0.35	0.35
7a	7882.8	4–13	8	1.8	0.36	1.03
7b	7873.9	4–13	16	2.7	0.75	0.71
7b	7876.4	14–20	16	2.5	0.83	0.53
7b	7879.3	14–20	16	2.4	0.25	0.70
7b	7881.0	14–20	16	2.3	1.64	0.83
7b	7883.0	14–20	16	2.2	1.48	0.47
7b	7885.6	14–20	16	2.1	1.49	0.41

Note. — Col(1): maser group number; Col(2): the best-fit velocity of the model maser component, with a typical uncertainty of 0.25 km s<sup>-1</sup>; Col(3): the epochs of the spectra used for fitting (for the dates see Table 1); Col(4): the reference epoch for velocity shown in Column(2); Col(5): the average linewidth; Col(6): the best-fit acceleration; and Col(7): the uncertainty of the acceleration. All fitted value come from acceleration fitting Method 1.

Table 4. NGC 6323 H<sub>2</sub>O Maser Model

Parameter	Priors	Posterioris	Units
$H_0$	...	$73^{+26}_{-22}$	km s <sup>-1</sup> Mpc <sup>-1</sup>
$V_0$	...	$7853.4^{+2.1}_{-2.2}$	km s <sup>-1</sup>
$V_p$	$-285^{+163}_{-163}$	$-282^{+190}_{-188}$	km s <sup>-1</sup>
$M$	...	$0.94^{+0.37}_{-0.26}$	$10^7 M_\odot$
$x_0$	...	$0.015^{+0.002}_{-0.002}$	mas
$y_0$	...	$0.011^{+0.002}_{-0.003}$	mas
$i_0$	...	$88.5^{+0.7}_{-0.6}$	deg
$di/dr$	...	$6.0^{+9.0}_{-6.2}$	deg mas <sup>-1</sup>
$p_0$	...	$189.5^{+0.2}_{-0.2}$	deg
$dp/dr$	...	$13.2^{+2.6}_{-2.6}$	deg mas <sup>-1</sup>

Note. — Parameters are as follows: Hubble constant ( $H_0$ ), recession velocity of the galaxy in optical convention relative to the Local Standard of Rest ( $V_{sys}$ ), peculiar velocity with respect to Hubble flow in cosmic microwave background frame ( $V_p$ ), black hole mass ( $M$ ), eastward ( $x_0$ ) and northward ( $y_0$ ) position of black hole relative to a conveniently chosen point close to the average position of all maser features, disk inclination ( $i_0$ ) and inclination warping (change of inclination with radius:  $di/dr$ ), disk position angle ( $p_0$ ) and position angle warping (change of position position angle with radius:  $dp/dr$ ). Flat priors were used, except where listed. Parameter values given in Table 4 were produced from binned histograms for each parameter. The quoted values here are the medians of the marginalized probability density functions, with the uncertainties showing the 16th and 84th percentiles (i.e., the 68% credible interval).

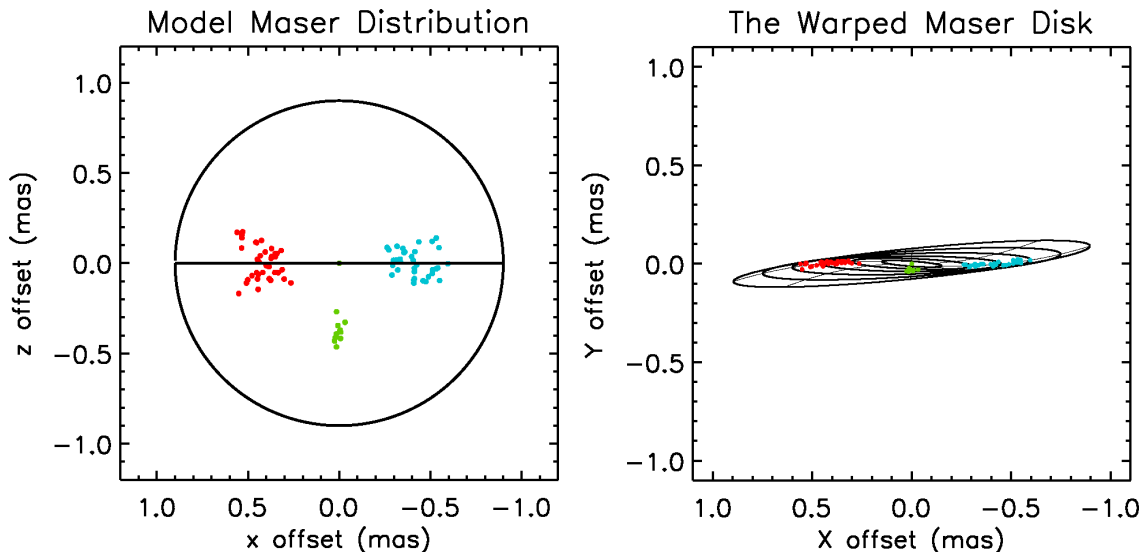


Fig. 6.— The left panel shows the maser distribution of our best-fit model for NGC 6323 from the overhead perspective. The right panel shows the best-fit model from the observer’s perspective with model maser spots plotted on top of the warp model. The red, green, and blue dots in both panels show the redshifted masers, the systemic masers, and the blueshifted masers, respectively. In the right panel, for the illustration purpose, we changed the observer’s viewing angle from  $89^\circ$  to  $83^\circ$  to show the degree of disk warping more clearly.

sensitivities the MCP should concentrate on sources with maser spots stronger than  $\approx 20$  mJy. However, if future radio telescopes can achieve significantly higher collecting areas and/or lower system temperatures, then we can make substantially better measurements for galaxies such as NGC 6323. We hope that the next generation Very Large Array will ultimately provide such an improvement.

## REFERENCES

- Braatz, J. A., Reid, M. J., Humphreys, E. M. L., Henkel, C., Condon, J. J., & Lo, K. Y. 2010, *ApJ*, 718, 657
- Felli et al. 2007, *A&A*, 476, 373
- Humphreys, E. M. L., Reid, M. J., Greenhill, L. J., Moran, J. M., Argon A. L. 2008, *ApJ*, 672, 800
- Kuo, C. Y., Braatz, J. A., Condon, J. J., Impellizzeri, C. M. V., Lo, K. Y., Zaw, I., Schenker, M., Henkel, C., Reid, M. J., Greene, J. E. 2011, *ApJ*, 727, 20
- Kuo, C. Y., Braatz, J. A., Reid, M. J., Condon, J. J., Lo, K. Y., Henkel, C., Impellizzeri, C. M. V. 2013, *ApJ*, 767, 155
- Masters, K. L. Ph.D dissertation, 2005. Section 0058, Part 0606 260 pages; United States – New York: Cornell University; 2005
- Reid, M. J., Braatz, J. A., Condon, J. J., Greenhill, L. J., Henkel, C., Lo, K. Y. 2009, *ApJ*, 695, 287
- Reid, M. J., Braatz, J. A., Condon, J. J., Kuo, C. Y., Impellizzeri, C. M. V., & Henkel, C. 2013, *ApJ*, 767, 154.



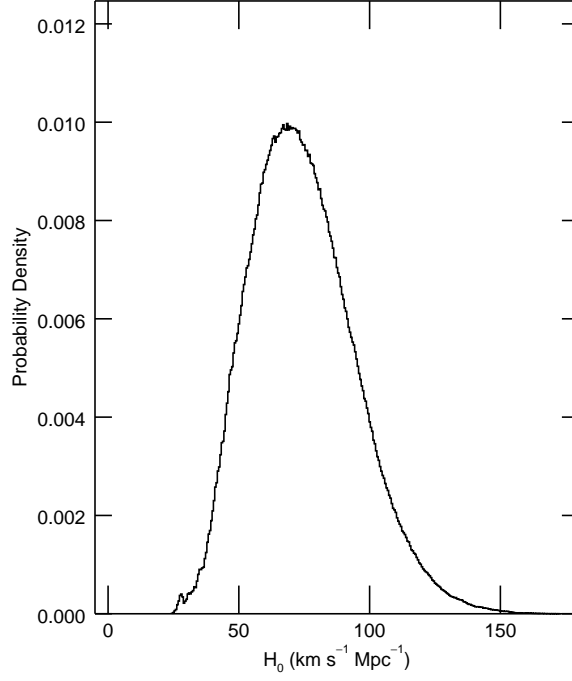


Fig. 7.— Marginalized posteriori probability distribution of the Hubble constant,  $H_0$ . The distribution for  $H_0$  has a median of  $73 \text{ km s}^{-1} \text{ Mpc}^{-1}$ , and the 16th and 84th percentiles are  $51 \text{ km s}^{-1} \text{ Mpc}^{-1}$  and  $99 \text{ km s}^{-1} \text{ Mpc}^{-1}$ , respectively. The peak of the distribution is at  $H_0 = 67 \text{ km s}^{-1} \text{ Mpc}^{-1}$ .